Earth and Planetary Science Letters 511 (2019) 36–43

Contents lists available at ScienceDirect

Earth and Planetary Science Letters

www.elsevier.com/locate/epsl

Fracture energy estimates from large-scale laboratory earthquakes

David S. Kammer *, Gregory C. McLaskey

School of Civil and Environmental Engineering, Cornell University, Ithaca, NY 14850, USA

ARTICLE INFO

Article history:
Received 29 August 2018
Received in revised form 15 January 2019
Accepted 18 January 2019
Available online 5 February 2019
Editor: M. Ishii

Keywords:
laboratory earthquake
fracture energy
fracture mechanics
rupture front
cohesive zone
strain oscillations

ABSTRACT

The dynamics of fault ruptures in natural and laboratory earthquakes is governed by a balance of released elastic energy and dissipated local fracture energy. The latter is the result of various friction weakening processes occurring at the fault and is thus often estimated indirectly and from small-scale friction experiments. We analyze high-frequency strain measurements from large-scale laboratory earthquakes with gages positioned slightly away from a granite fault. The strain measurements present rapid fluctuations during fault rupture propagation, as was also observed in other experiments. Characteristics of these strain fluctuations are compared with fracture mechanics theory to estimate local fault properties. We determine fracture energy for secondary rupture fronts, which appear behind the main front where local slip occurred already. Measured fracture energy is consistent with indirect estimates from rupture termination in independent experiments but is orders of magnitude lower than reported values from rotary shear friction experiments, which may be due to large differences in overall slip.

1. Introduction

The determination of fault properties such as weakening processes and friction parameters are important issues to earthquake mechanics as they directly affect how earthquakes initiate, grow, and stop. However, measurements of local fault properties such as stress state and frictional strength have been prohibitively difficult. Small-scale laboratory rock experiments are a useful approach to study friction and have produced a number of insights including rate-and-state friction (Dieterich, 1979; Ruina, 1983), and additional weakening processes that take place at ∼m/s slip rate (Di Toro et al., 2011). Other experiments – so-called laboratory earthquakes – provide insight into dynamic rupture processes including supershear (Xia et al., 2004; Svetlizky et al., 2016; Kammer et al., 2018) and pulse-like (Lykotrafitis et al., 2006; Lu et al., 2007) rupture propagation, nucleation (Okubo and Dieterich, 1984; Ohnaka and Kuwahara, 1990; Mitiyasu and Lin-feng, 1999; McLaskey and Kilgore, 2013; Latour et al., 2013), and rupture arrest (Rubinstein et al., 2007; Bayart et al., 2016). It remains unclear, however, how these laboratory observations should be scaled to the size and rates of naturally occurring earthquake fault ruptures. We aim to quantify properties of the laboratory earthquakes in order to establish a quantitative link between the small-scale experiments and larger natural earthquake rupture processes.

Fracture energy has been recognized as an important factor related to the fault weakening process and has been used for determining seismic efficiency and the overall energy budget of an earthquake (Beeler et al., 2012; Nielsen et al., 2016a,b). It is possible to constrain fracture energy from seismic observations (Abercrombie and Rice, 2005; Guatteri and Spudich, 2000; Tinti et al., 2005), and appears to be a relatively stable dynamic earthquake parameter. It is important to note that the term fracture energy has been used with somewhat different definitions in different contexts. Seismological estimates of fracture energy are usually global quantities – averages over the entire rupture area and duration of the earthquake (Beeler et al., 2012). In contrast, this and other work describes local fracture energy of a specific fault patch. A full reconciliation of the various forms of fracture energy is outside the scope of this work. Instead, we describe methods for determining local fracture energy that are consistent with an engineering fracture mechanics definition (Freund, 1990), with the hopes of establishing an energy-based mathematical framework that uses local stress state and friction properties to enable quantitative predictions of rupture initiation, propagation, and arrest [*e.g.*, Ke et al. (2018)]. By further exploring these processes at the laboratory scale, we hope to eventually link this engineering understanding of fracture mechanics to the earth science view of the earthquake rupture process.

In this work, we utilize a theoretical fracture mechanics framework with a cohesive crack model to determine local fracture energy and its relationship to the rupture velocity and rupture extent. Building upon recent work on glassy polymers

* Corresponding author.
E-mail address: kammer@cornell.edu (D.S. Kammer).

https://doi.org/10.1016/j.epsl.2019.01.031
0012-821X/

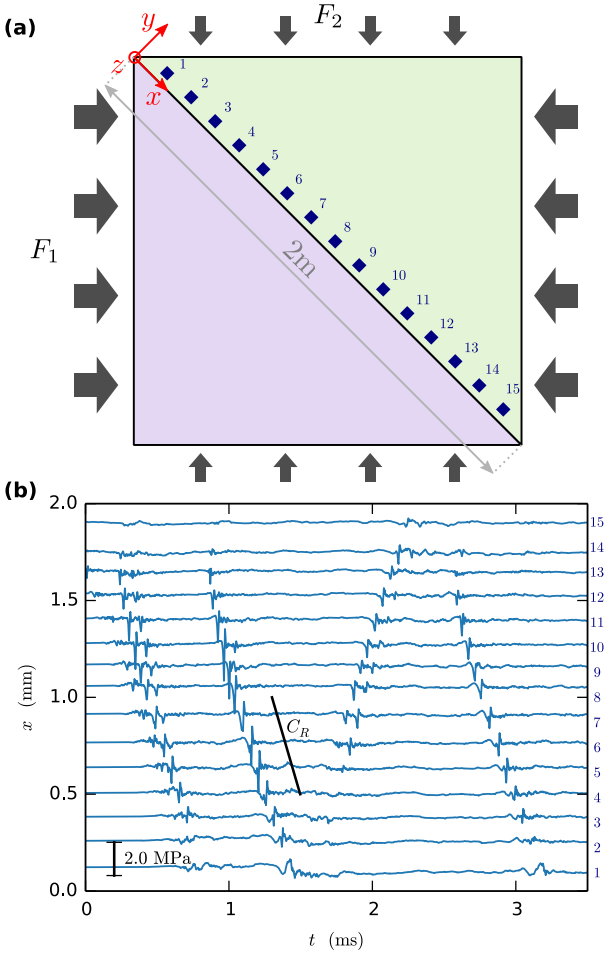

Fig. 1. Experimentally observed rupture fronts in large-scale laboratory earthquakes. (a) Set-up for laboratory experiments at the U.S. Geological Survey. Two granite samples are loaded by normal forces F_1 and F_2 and create a simulated fault that is under combined shear and normal load. Fault ruptures nucleate naturally and propagate along the fault at $y = 0$. Local shear stress is measured with 15 strain gage pairs along and slightly offset from the fault (blue squares). (b) Example measurements of shear stress observed during a laboratory earthquake show oscillations indicating the presence of rupture fronts. Shear stress evolution are shown at x-position along fault with amplitude according to scale. Rupture fronts propagate at speeds slightly below the Rayleigh-wave speed C_R and are often reflected at the fault edges. (For interpretation of the colors in the figure(s), the reader is referred to the web version of this article.)

(Svetlizky and Fineberg, 2014) showing a singular stress field around slip fronts, we study rupture fronts from laboratory earthquakes generated on a 2-meter granite sample originally reported in McLaskey et al. (2015). Focusing on secondary rupture fronts, described below, we demonstrate how to apply fracture mechanics theory to estimate local fracture energy and cohesive zone size from local stress measurements.

2. Methods

2.1. Laboratory experiments

The experiments were performed on the biaxial apparatus at the USGS in Menlo Park, California. The simulated fault is a 2 m long diagonal saw cut between two granite slabs (Dieterich, 1981; Okubo and Dieterich, 1984; McLaskey et al., 2015), as shown schematically in Fig. 1a. The fault surface was initially roughened to 80 μm peak-to-trough roughness, but has likely been smoothed somewhat from the decades of experiments on the same samples. Using servo control, the applied forces F_1 and F_2 evolved slowly such as to maintain a constant normal stress $\sigma_{yy} \approx 6$ MPa and increasing shear stress σ_{xy} at a rate of 0.001 or 0.01 MPa/s. When the sample reached a critical stress level, a laboratory earthquake nucleated naturally.

The two granite samples form a fault with dimensions $x = 2$ m and $z = 0.4$ m. The dynamic elastic properties of granite, $E = 51$ GPa and Poisson's ratio $\nu = 0.25$, were deduced from measured longitudinal wave speed $C_d \approx 4790$ m/s, shear wave speed $C_s \approx 2760$ m/s and density $\rho = 2670$ kg/m^3 (McLaskey et al., 2015). The Rayleigh-wave speed is $C_R \approx 2540$ m/s.

The shear strain along the fault was recorded with 15 high-frequency strain gage pairs that were positioned at $y \approx 13$ mm from the trace of the fault. While measurements directly on the fault are desired, they are not practical due to the finite size of the gages. This off-fault position affects the observed strain (see section 2.2). Strain was then converted to stress through elastic relations. The shear stress measurements presented important fluctuations during the course of a laboratory earthquake and reveal the propagation of rupture fronts (Fig. 1b). The propagation speed of these rupture fronts C_f was measured by tracking the minimum of the shear stress fluctuation and computing $C_f = dx/dt$, where dx is the distance between two strain gages and dt the time delay of strain-fluctuation occurrence.

During a single laboratory earthquake, multiple fronts may occur and they are often reflected at the fault edges. We name these events *secondary rupture fronts* as they propagate along parts of a fault where a first *primary rupture front* has already caused local slip. In these experiments, the primary rupture fronts propagated slowly (20–400 m/s, $0.01 < C_f/C_R < 0.16$), were associated with nucleation, were outside the high speed recording time window, and are not shown in Fig. 1b. Most of the studied secondary rupture fronts propagated at sub-Rayleigh speeds, in the range of $0.85 < C_f/C_R < 0.99$. Similar secondary rupture fronts have been observed in other experiments (Xu et al., 2017) but have not been analyzed.

2.2. Fracture mechanics model with cohesive zone

The stress state around a rupture front, which is essentially a shear crack, can be described by dynamic Linear Elastic Fracture Mechanics (LEFM) theory (Svetlizky and Fineberg, 2014). The change in the near-tip stress field of a singular shear crack (Freund, 1990) is given in polar coordinates (r, θ) by

$$\Delta\sigma_{xy}(\theta, r, C_f) = \frac{K_{\mathrm{II}}(C_f)}{\sqrt{2\pi r}}\, \Sigma^{\mathrm{II}}_{xy}(\theta, C_f)\,, \tag{1}$$

where K_{II} is the stress intensity factor and $\Sigma^{\mathrm{II}}_{xy}$ the angular variation. Describing the change of stress with LEFM theory despite residual friction is possible due to the linearity of the governing equations of mode II cracks when shear stress is expressed relative to σ^r_{xy} by $\Delta\sigma_{xy} = \sigma_{xy} - \sigma^r_{xy}$. A detailed summary of all relevant terms in Eq. (1) is provided in Appendix A.

How is the off-fault stress measurement related to local friction properties? K_{II} can be related to the fracture energy Γ through an energy balance with the dynamic energy release rate G_{II} by

$$\Gamma = G_{\mathrm{II}} = \frac{(1-\nu^2)}{E}\, K^2_{\mathrm{II}}\, f_{\mathrm{II}}(C_f)\,, \tag{2}$$

where $f_{\mathrm{II}}(C_f)$ is a known universal function of crack speed (Appendix A). Solving Eq. (2) for K_{II} and substituting into Eq. (1) allows us to express the near-tip stress field as a function of Γ, which is assumed to be an interface property. The near-tip stress field is also a function of C_f, which is discussed in a later section.

A similar solution can be found for the more general case of a cohesive crack, which regularizes the elastic singular fields at the rupture tip. A cohesive crack presents a process zone, in which

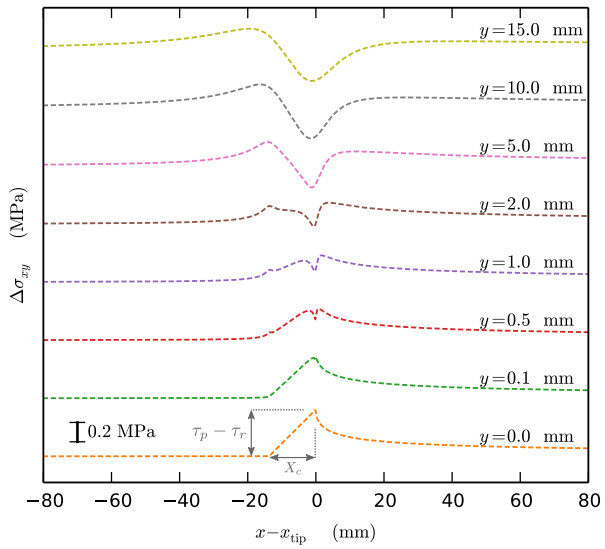

Fig. 2. Shear stress fluctuation of a cohesive crack at various off-fault distances. The shear stress evolution $\Delta\sigma_{xy}$ is shown as function of rupture tip position. On fault ($y = 0$ mm) $\Delta\sigma_{xy}$ reaches its peak value at the rupture tip. It then decreases over the size of the cohesive zone X_c. With increasing distance to the fault ($y > 0$), $\Delta\sigma_{xy}$ changes shape and presents the typical oscillatory stress evolution as observed in experiments. The presented example propagates at $C_f = 2404$ m/s and has $\Gamma = 0.21$ J/m^2 and $X_c = 13.8$ mm.

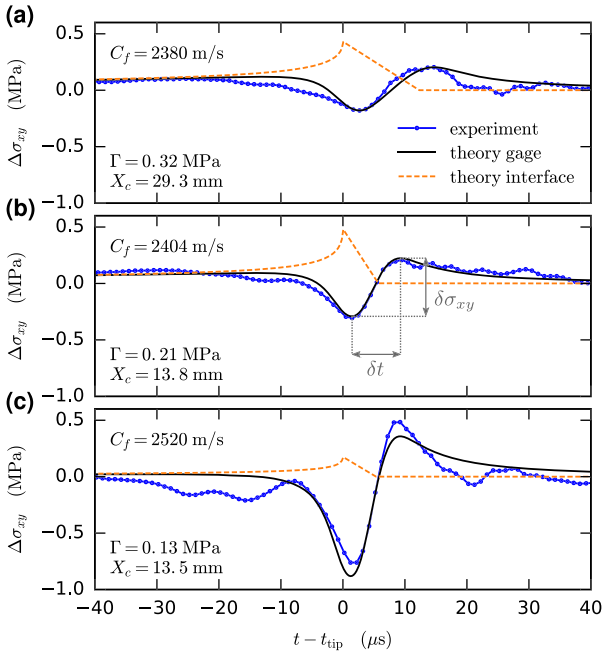

Fig. 3. Examples of measured shear stress oscillations with comparison to fracture-mechanics based model. Three examples of experimentally measured shear stress evolution $\Delta\sigma_{xy}$ relative to rupture tip arrival with different oscillation amplitudes $\delta\sigma_{xy}$ are shown in blue. Fracture-mechanics based model that incorporates shape and position of strain gage pairs is depicted by black curve. The associated shear stress evolution at the fault ($y = 0$) is shown in dashed orange. The theoretical near-tip stress fields were transformed from space to time and are therefore reversed compared to curves shown for space in Fig. 2.

the shear stress is limited by the peak strength τ_p and reduces to the residual stress τ_r over a characteristic length scale – the cohesive zone size X_c. However, the simple separation of stress intensity factor and angular variation is lost in the cohesive-crack solution, and the stress variation is expressed through complex variables (Poliakov et al., 2002; Samudrala et al., 2002). Detailed equations are given in Appendix A. The stress field around a cohesive crack depends on the crack speed, the local fracture energy Γ, the size of the cohesive zone X_c, and the spatial stress distribution within the cohesive zone. Due to unknown stress distributions, we apply a linear cohesive zone as a first approximation. While this approach might be simplistic, it provides valuable insight into the mechanics of these laboratory earthquakes. The stress distribution $\Delta\tau(\xi) = \tau(\xi) - \tau_r$ in local coordinates $\xi = x - x_{tip}$ around the position of the crack tip x_{tip} is given by:

$$\Delta\tau(\xi) = \begin{cases} 0 & \xi < -X_c \\ (1 + \xi/X_c)(\tau_p - \tau_r) & -X_c < \xi < 0. \end{cases} \quad (3)$$

3. Results

We apply the fracture-mechanics-based theoretical framework to analyze the observed stress fluctuations in the experiments. This provides a link between fault friction properties and stress state near the rupture front. We first compare experimental measurements of stress fluctuations with fracture mechanics descriptions. We then use the analytic model to demonstrate how the stress distribution along the fault affects these off-fault stress fluctuations and provide an interpretation of reported experimental observations. Finally, we present a link between the fracture energy and the dynamics of these rupture fronts.

3.1. Shear stress fluctuation comparison

The theoretical shear stress field along the fault for a cohesive crack is shown by a dashed orange curve in Fig. 2 ($y = 0$ at bottom). Approaching the rupture tip at x_{tip}, the shear stress increases, reaches the peak strength τ_p of the fault, decreases within the process zone of length X_c and finally reaches τ_r. The shear tractions at the fault are reported relative to the residual friction through $\tau - \tau_r$. First order fracture mechanics theory describes variations in the near-tip stress fields but has no permanent stress change far from the rupture tip, *i.e.*, $\tau \to \tau_r$ for $x - x_{tip} \gg 0$. The off-fault position of the strain gages ($y \neq 0$) and the angular dependence of the near-tip stress field, as given by Eq. (1) for a singular crack, transform the stresses observed along the fault into an oscillatory stress evolution as described for a cohesive crack in Fig. 2.

Fig. 3 shows close-ups of three stress fluctuation examples (blue curves) from Fig. 1b. As was noted for the theoretical data, the shear stress is reported relative to the residual stress as $\Delta\sigma_{xy} = \sigma_{xy} - \sigma^r_{xy}$, where σ_{xy} is the measured stress and σ^r_{xy} is the residual stress. σ^r_{xy} is determined as average over the time interval 40 μs $\leq t - t_{tip} \leq$ 50 μs, where t_{tip} is the time of rupture front arrival. The main oscillation of the shear stress fluctuation presents a very distinct shape that is common to most fluctuations observed in the experiments. The shear stress is initially ($t - t_{tip} \ll 0$) at the pre-stress level σ^0_{xy}. As the rupture tip approaches, the stress decreases before it increases quickly (even above σ^0_{xy}) and finally decreases again to σ^r_{xy}. Similar shear stress oscillations have also been observed in other experimental setups (Svetlizky and Fineberg, 2014; Fukuyama et al., 2016; Xu et al., 2017; Rubino et al., 2017).

The theoretical solution at $y \approx 13$ mm (theory gage) compares quantitatively well to the measured shear stress fluctuations as shown by black lines in Fig. 3. For comparison with strain–time measurements from the experiments, we transform the near-tip stress field to time through $\Delta\tau(t) = \Delta\tau(-x/C_f)$, which assumes constant crack speed C_f. Effects of the gage set-up (*i.e.*, pair offset and finite size) are considered by spatial averaging of the strain field and the gage bandwidth is approximated by applying a 500 kHz low-pass butterworth filter. The main averaging contri-

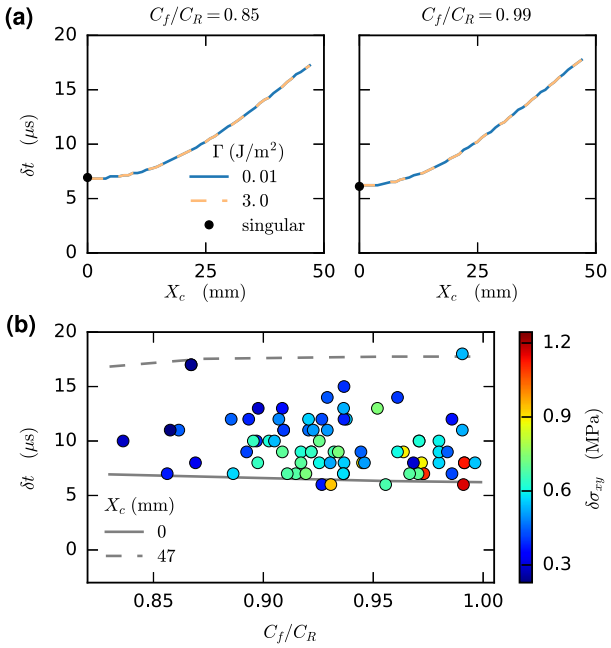

Fig. 4. Effect of fracture energy Γ and cohesive zone size X_c on duration of shear stress oscillations observed in strain gage measurements. (a) Oscillation duration δt, as defined in Fig. 3, with respect to cohesive zone size is shown for rupture speed $C_f/C_R = 0.85$ (left) and 0.99 (right) for $\Gamma = 0.01$ and 3 J/m^2. The prediction for a singular crack approximation is marked by black point. (b) Characterization of experimentally measured shear stress oscillations. Measured oscillation time is reported as a function of rupture speed. Color indicates measured oscillation amplitude. Gray lines indicate fracture-mechanics-based prediction of δt for singular crack tip (solid) and cohesive crack with $X_c = 47$ mm (dashed).

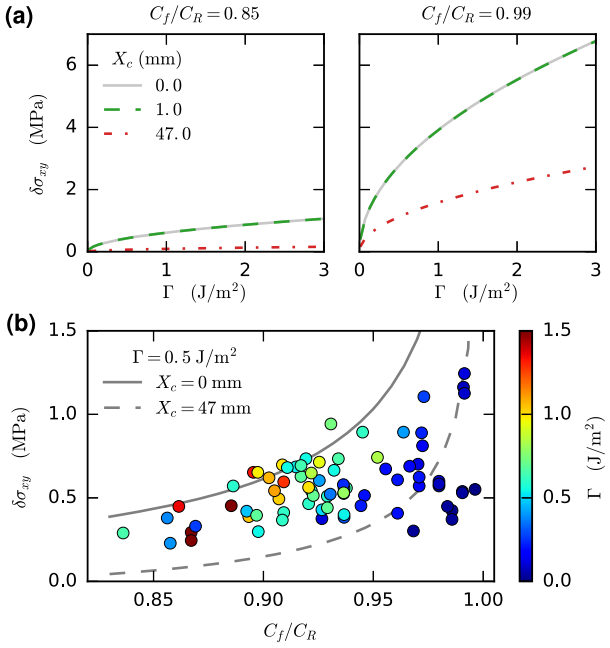

Fig. 5. Effect of fracture energy Γ and cohesive zone size X_c on amplitude of shear stress oscillations observed in strain gage measurements. (a) The effect of fracture energy on the oscillation amplitude $\delta\sigma_{xy}$, as defined in Fig. 3, is shown for singular and cohesive cracks with $X_c = 1$ and 47 mm for rupture speed $C_f/C_R = 0.85$ (left) and 0.99 (right). (b) Characterization of experimentally measured shear stress oscillations. Measured oscillation amplitude is depicted with respect to rupture speed. The associated fracture energy is shown in color. Gray lines indicate fracture-mechanics theory of $\delta\sigma_{xy}$ for $\Gamma = 0.5$ J/m^2 for singular crack (solid) and cohesive crack with $X_c = 47$ mm (dashed).

bution is due to the pair offset and the finite size of the gages. The effect of the bandwidth is minor.

This comparison was also shown by Svetlizky and Fineberg (2014) for friction experiments on poly(methylmethacrylate) (PMMA). The parameter choice of the interface properties applied for this comparison is discussed later in this article. It is important to note that there is no direct evidence of the peak strength observable on the strain gage measurements even though they are only ≈ 13 mm from the fault. In fact, the off-fault stress decreases where the on-fault stress reaches its peak. An initial stress increase in the off-fault measurements as reported by Svetlizky and Fineberg (2014) and McLaskey et al. (2015) can occur due to non-steady phenomena such as waves caused by initial nucleation (Svetlizky et al., 2016).

3.2. Interface characterization

The observed stress fluctuations measured by the strain gages vary in amplitude and duration. Different values for Γ and X_c were used to achieve good agreement with fracture mechanics theory for the examples shown in Fig. 3. This provides us with the opportunity to use the properties of the stress fluctuations to characterize the frictional behavior of the fault. As shown in Fig. 3, we define δt and $\delta\sigma_{xy}$ as the duration and amplitude of the stress fluctuation, respectively. In Fig. 4a and Fig. 5a, we analyze the effect of Γ and X_c, the only parameters of the linear cohesive zone, on δt and $\delta\sigma_{xy}$.

Fig. 4a shows that δt is minimal for a singular crack and increases with X_c. The quantitative values are a result of the strain gage set-up and would be different for other geometries. The presented $X_c - \delta t$ relation is shown for $C_f/C_R = 0.85$ and 0.99, which are the lower and upper limit of rupture speeds analyzed here, respectively, but is representative for all intermediate rupture speeds. Furthermore, δt is independent of Γ. Thus, we can use the measurement of δt to determine the cohesive zone size X_c. In addition, δt is insensitive to C_f as shown by gray curves in Fig. 4b. Uncertainties in the measurements of the crack speed are therefore not carried over into the X_c estimations.

Fig. 4b presents δt for 77 stress oscillations from 14 rupture fronts in 5 different experiments. Also shown is the theoretical prediction for a singular crack ($X_c = 0$) calculated using the geometry of the strain gages. The lower limit of measured δt over the entire range of crack speeds is consistent with this independent theoretical prediction. This supports the validity of our approach. The data along the lower limit indicate that the cohesive zone size for these rupture fronts is likely $X_c < 10$ mm as they are virtually indistinguishable from a singular crack with our strain gage set-up [$\delta t(X_c = 0) \approx \delta t(X_c = 10$ mm) as shown in Fig. 4a]. The maximal cohesive zone size observed is $X_c \approx 47$ mm.

Fracture mechanics predicts a contraction of X_c with C_f for uniform systems with constant interface properties, *i.e.*, $\tau_p - \tau_r$ and Γ. This contraction has been observed in similar experiments on PMMA (Svetlizky and Fineberg, 2014). Our experimental data, however, does not present a correlation between C_f and δt, as shown in Fig. 4b, and thus does not show the contraction. We believe that the heterogeneous nature of the experiments presented here cause enough variation that hide the expected contraction.

After using δt to determine X_c, we now focus on the stress oscillation amplitude $\delta\sigma_{xy}$ and local fracture energy Γ. Fig. 5a presents $\delta\sigma_{xy}$ as a function of Γ for various X_c. For a singular crack it goes $\delta\sigma_{xy} \sim \sqrt{\Gamma}$. Cohesive cracks follow the same $\sqrt{\Gamma}$ shape but present lower $\delta\sigma_{xy}$ for increasing X_c. Further, $\delta\sigma_{xy}$ increases with C_f for singular and cohesive cracks (see Fig. 5b).

Measurements of $\delta\sigma_{xy}$ as a function of C_f are presented in Fig. 5b. A unique relation would be expected if X_c and Γ were constant. We do not observe such a relation because we have a

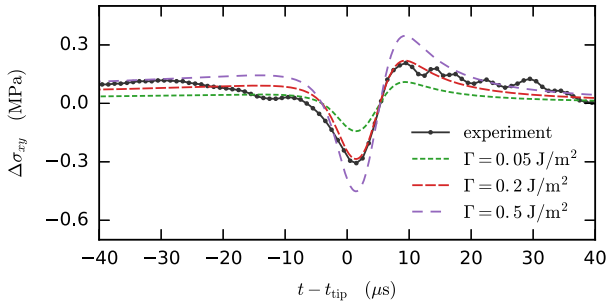

Fig. 6. Illustration of fracture energy determination process by amplitude comparison of shear stress oscillation. Oscillation amplitude $\delta\sigma_{xy}$ as defined in Fig. 3b is used to compare fracture mechanics prediction with experimental observation. Monotonic relation between $\delta\sigma_{xy}$ and fracture energy Γ, as shown in Fig. 5a, allows to determine local Γ when cohesive zone size X_c and rupture velocity are known. Presented example corresponds to rupture front shown in Fig. 3b that propagates at $C_f = 2404$ m/s and has $X_c = 13.8$ mm.

range of X_c, as determine by δt. Considering X_c, we measure Γ through comparison of $\delta\sigma_{xy}$ with theory as illustrated in Fig. 6. Values of Γ for all analyzed stress oscillations are shown as color map in Fig. 5b. We observe a range of $\Gamma = 0.014$–3.0 J/m^2 and note an overall relation between Γ and C_f. Higher Γ occur for ruptures at lower speed. Nevertheless, the relation between Γ and C_f is not prefect (see color map in Fig. 5b), which confirms previous observations of heterogeneity in the system. Furthermore, we find 0.1 MPa $< \tau_p - \tau_r <$ 2.6 MPa (using Eq. (A.12) from Appendix A), which is another indicator of the presence of heterogeneity.

3.3. Rupture front dynamics

We now focus on the dynamics of these rupture fronts. Fig. 7a presents the crack speed as function of crack length l, where l is the distance from the rupture tip to the trailing edge of the sample. We observe rupture fronts accelerate and decelerate as they propagate. Independent of l and position x, the rupture may propagate at any of the observed rupture speeds. Moreover, fracture energy appears to be independent of crack length (Fig. 7b). However, as also shown in Fig. 5b, lower Γ are associated with faster rupture fronts. Note how in Fig. 7b the orange and green rupture fronts slow down simultaneously with increased Γ.

The same data falls into a narrow range when C_f is plotted with respect to l/Γ (Fig. 7c). Low C_f occur for low l/Γ whereas high C_f can be observed for a large range of l/Γ (*i.e.*, $C_f/C_R > 0.97$ for $8 < l/\Gamma < 70$). Rupture fronts on PMMA samples have been shown to follow the LEFM equation of motion (Svetlizky et al., 2017), which states, assuming time-invariant loading, that C_f/C_R is a function of G^s_{II}/Γ, where G^s_{II} is the static energy release rate. Further assuming a constant dynamic stress drop $\tau_0 - \tau_r$ along the interface, we know that $G^s_{\text{II}} \sim (\tau_0 - \tau_r)^2 l$. Theoretical predictions for various $\tau_0 - \tau_r$ are shown in Fig. 7c.

With the exception of two data points, all data is comprised by $\tau_0 - \tau_r = 0.08$–0.25 MPa. Furthermore, the theory shows clearly why low C_f/C_R values can only be observed for low l/Γ but very fast rupture fronts can occur for a large range of l/Γ values. Note in particular that the highlighted rupture fronts cover large ranges of C_f and Γ and are all within the band of our theoretical prediction.

4. Discussion

4.1. Secondary rupture fronts

Natural earthquakes are conceptually considered being a rupture front that nucleates at the hypocenter, propagates along the fault and finally arrests. Recent seismic observations (Ishii, 2011; Meng et al., 2011, 2015), however, present a much more complicated process. The total amount of fault slip, which directly affects the magnitude of the earthquake, is not only the result of the main rupture but is also caused by other fronts, similar to secondary rupture fronts observed in the experiments. These secondary fronts are also a source of high-frequency radiation in natural earthquakes (Meng et al., 2011) and in laboratory earthquakes (McLaskey et al., 2015), and contribute to the resulting natural hazard. Other secondary fronts appear as foreshocks during the slow nucleation process of natural earthquakes (Meng et al., 2015) and have also been observed in laboratory experiments (McLaskey and Kilgore, 2013). Characterizing the mechanics of these secondary fronts and the fault properties related to these mechanisms is important to make better models of earthquake complexity (Galvez et al., 2016). Our proposed methodology allows us to provide insight into these secondary rupture fronts, which would not be possible with standard small-scale friction experiments without rupture fronts. A similar approach was applied to primary rupture fronts in Svetlizky and Fineberg (2014).

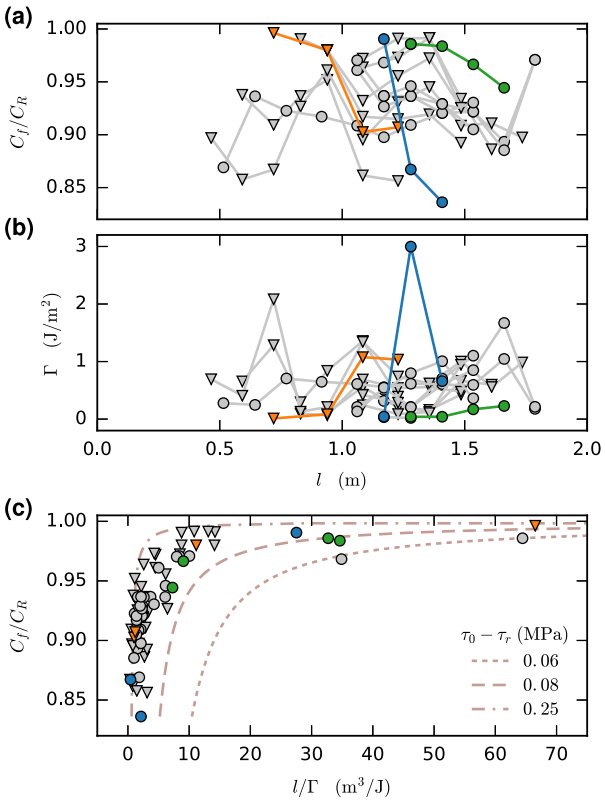

Fig. 7. Dynamics of rupture fronts at granite fault. (a) Rupture speed is shown as crack length l increases. Circle and triangle markers indicate right and left propagating rupture fronts, respectively. Various propagation patterns are observed with rupture fronts accelerating and decelerating. Three cases are highlighted in color. (b) Estimated fracture energy, $\Gamma = 0.01$–3.0 J/m^2, is reported for same rupture fronts as shown in (a). (c) Rupture speed as a function of l/Γ. Fracture-mechanics based equation of motion (Svetlizky et al., 2017) provides frame for experimental data with dynamic stress drop $\tau_0 - \tau_r$ being the only free parameter (brown lines). Experimental data is within fracture-mechanics predictions for $0.08 < \tau_0 - \tau_r < 0.25$ MPa with only two points lying on $\tau_0 - \tau_r = 0.06$ MPa. Highlighted examples illustrate extent of observed data.

4.2. Fracture mechanics model assumptions

The fracture-mechanics theory we applied to analyze experimental data is based on several important assumptions. One such assumption is the time-invariant stress state. While the primary rupture front is likely unaffected by reflected elastic waves due to

the size of the granite samples, secondary rupture fronts are possibly interacting with a dynamic stress field. This is one possible source for the range of $\tau_0 - \tau_r$ shown in Fig. 7c. Nevertheless the observed behavior is within a reasonable small range of values, which supports our approach.

Other important assumptions are the linear stress distribution within the cohesive zone and constant residual friction. The link between the cohesive zone model with $\Delta\tau(\xi)$ as given by Eq. (3), and local friction laws that describe frictional strength $\Delta\tau(\delta, \dot{\delta}, \theta, ...)$ as function of local slip δ, slip rate $\dot{\delta}$ and state θ is non-trivial and requires numerical results. Similarly, effects of non-constant residual stress due to rate dependence or time-dependent healing cannot be included directly into our theoretical model. Better prediction based on realistic friction laws would require numerical simulations to determine the near-tip stress field for various rupture speeds. The applied model is therefore a first approximation to determine order of magnitudes for X_c and Γ. Extensions based on rate-and-state friction laws (Dieterich, 1979; Ruina, 1983) could explain the range of values for X_c and Γ (see Fig. 4 and 5) and the observed heterogeneity, but might also give similar results (Bizzarri and Cocco, 2003).

Our analysis of off-fault strain measurements could also be affected by off-fault inelastic processes that are neglected in this work. Early simulations (Rice, 2005; Poliakov et al., 2002) have shown that dynamic shear ruptures can cause considerable off-fault plasticity near the fault and create a so-called low-velocity zone. In this area, the elastic modulus of the material is reduced. These effects are even stronger for rough faults (Dunham et al., 2011; Shi and Day, 2013). If the low-velocity fault zone extended until the position of the strain gages ($y \approx 13$ mm), it would directly affect the elastic relations applied here to determine stresses from strain measurements. Whether such off-fault inelastic processes occur in the current experiments is difficult to evaluate. While we do not have any obvious indicators, we believe, based on estimated slip rates of $\sim$ 200–400 mm/s (McLaskey et al., 2015), that some off-fault damage could occur in these experiments.

Furthermore, current measurements from these laboratory earthquakes (McLaskey et al., 2015) are inconclusive on whether the fault is continuously sliding between two consecutive secondary events. If the fault stops sliding before the next event approaches, these secondary rupture fronts are essentially equivalent to primary fronts but with a much shorter healing time. It could therefore be expected that they are described by fracture mechanics theory, as are primary rupture fronts (Svetlizky and Fineberg, 2014). However, the analogy is considerably less trivial and intuitive if continuous sliding occurs, as it would be equivalent to a crack propagating through a cracked area. Consequently, simple slip-dependent friction laws would not explain this behavior, which would be another reason to adapt our approach to use rate-and-state friction laws. Our results, however, suggest that fracture-mechanics theory appears to describe well these secondary rupture fronts even though they might not be classical ruptures that transition an interface from sticking to sliding but propagate along an already sliding fault.

4.3. Fracture energy

The fracture energy Γ is an important property for rupture front dynamics and earthquakes as it directly affects rupture speed (Svetlizky et al., 2017) and arrest (Kammer et al., 2015; Bayart et al., 2016; Ke et al., 2018). We find $\Gamma = 0.01$–1.5 J/m^2 for most of our data (Γ can exceptionally go up to 3.0 J/m^2) which is at the lower end of values $\Gamma = 0.2$–3.5 J/m^2 reported in similar experiments on granite where Γ was constrained by arrest locations of primary rupture fronts (Ke et al., 2018). This suggests that secondary rupture fronts reach similar levels of fracture energy as primary rupture fronts with a slight tendency to lower values – probably due to the interface being already weakened by the primary rupture front. Similar but somewhat higher values for Γ were also observed in PMMA experiments (Bayart et al., 2016).

A fracture energy quantity can also be determined with a different approach, which is based on (small-scale) rotary shear friction experiments (Nielsen et al., 2016a). In this approach, a stress-slip weakening curve is directly measured and used to estimate fracture energy. These experiments show that frictional weakening continues to occur with increasing slip, even for >0.01 m. As a result fracture energy is found to increase with increasing slip, consistent with seismic estimates (Viesca and Garagash, 2015; Abercrombie and Rice, 2005). Estimates based on the rotary shear experiments ranged from 100 J/m^2 at 1 mm of slip up to 10^6 J/m^2 at 1 m of slip, orders of magnitude larger than the values found in our laboratory experiments and those mentioned in the previous paragraph. For the current experiments, the fault slip during secondary rupture fronts is only 2–4 μm (McLaskey et al., 2015) so our fracture energy estimates ($\Gamma = 0.01$–1.5 J/m^2) are roughly consistent with the Γ slip scaling suggested by previous studies (Nielsen et al., 2016a; Viesca and Garagash, 2015; Abercrombie and Rice, 2005).

An important question is whether Γ depends on rupture speed and/or slip rate (Chang et al., 2012). To answer this question, we would need a clear relation between $\Delta\sigma_{xy}$ and C_f/C_R, to which we could fit the prediction from fracture-mechanics based on a rate-dependent Γ. Our data, as shown in Fig. 5b, does not outline such a relation. The observed trend of lower Γ for higher C_f/C_R and vice versa, could simply be the effect of local heterogeneity. When a rupture front enters a zone of low Γ, the rupture accelerates following the dynamics presented in Fig. 7c. The difficulty of determining a $\Gamma - C_f/C_R$ relation is further aggravated by the fact that we observe a wide range of X_c. The fracture-mechanics description in Fig. 7c depends on both Γ and X_c, which contributes to the dispersion of data points and the complexity of interpretation.

A limiting factor for the interpretation of the experiments is the strain gage design. As shown by Fig. 4a, we can only determine reliably X_c down to approximately 10 mm with the current system. Smaller X_c leads to δt that are indistinguishable from the value for singular crack tips. Improved data could be recorded by placing the strain gages closer to the fault (*i.e.*, smaller y) and using smaller strain gages. The 500 kHz bandwidth does not seem to be limiting in the current set-up.

4.4. Rupture front dynamics and crack versus slip pulse

What determines the propagation speed of these rupture fronts? While Fig. 7a–b show that the range of rupture speeds is large for any position at the fault and any crack length, which could suggest insensitivity to x and l, there appears to be an effect of Γ on C_f. Fig. 7c illustrates a more complete picture of rupture speed. It clearly depends on l and Γ as well as the dynamic stress drop $\tau_0 - \tau_r$ (and so indirectly to the prestress), as shown by fracture-mechanics theory. However, it is interesting to note that C_f is much more sensitive to all of these properties at relatively short crack lengths, *i.e.*, small l/Γ. Small changes in l, Γ and $\tau_0 - \tau_r$ considerably affect C_f for small l/Γ. At relatively large crack lengths, C_f becomes almost independent of all three properties and is generally close to C_R.

The applied theory and the analyzed data is limited to rupture fronts that propagate slower than the Rayleigh wave $C_f < C_R$. The near-tip stress fields around supershear cracks ($C_f > C_s$) are fundamentally different (Broberg, 1989, 1994; Samudrala et al., 2002; Dunham and Archuleta, 2005; Bhat et al., 2007; Mello et al., 2010)

and would require the appropriate theoretical approach for meaningful interpretation of experimental observations.

Despite numerous limitations, our approach and analysis provides useful insights into the properties of the fault and secondary rupture fronts. For instance, we provide an estimation of the local fracture energy, a fault property that is extremely important but very difficult to measure experimentally. We also show that these secondary rupture fronts seemed to be governed by the same mechanics as "normal" rupture fronts that rupture the interface and shear cracks, but may present a lower fracture energy. It is also interesting to note that the rapid stress oscillations as observed in Figs. 1b and 3 have in the past been interpreted as an indicator for slip pulses. The fracture-mechanics theory applied here, however, assumes a crack-like behavior and results in stress oscillations that are quantitatively equivalent to experimental measurements. Theory for pulse-like ruptures (Rice, 2005) present the same near-tip stress field as crack-like ruptures when the pulse is large enough compared to the cohesive zone ($>\approx 3X_c$) and therefore slip pulses are indistinguishable from cracks when analyzing stress measurements.

5. Conclusion

Laboratory-generated earthquakes are an important tool to study the underlying mechanics of natural earthquakes that exhibit complex behavior. We analyzed data from experiments (McLaskey et al., 2015) that present secondary rupture fronts propagating within a sliding fault. These events could be analogous to rapidly propagating events within an overall slower natural earthquake (Ishii, 2011; Meng et al., 2011, 2015). We showed that the stress oscillations observed for these secondary events are quantitatively well described by the near-tip stress field of a cohesive zone model for shear cracks. These stress oscillations do not resemble the stress along the fault but can be analyzed to determine fault properties. We estimated the fracture energy to be 0.01–3.0 J/m^2, which appears to be similar but with a tendency of lower values compared with primary rupture fronts reported in literature. We further showed that the secondary rupture fronts propagate at speeds that are consistent with fracture mechanics based predictions and suggest that the underlying mechanics is equivalent to a shear crack even though these events propagate along an interface that is potentially already sliding.

Acknowledgements

We thank Mathilde Radiguet for helpful discussions. We also thank editor Miaki Ishii and three anonymous reviewers for their helpful reviews. This work was partially funded by USGS Earthquake hazards grant G18AP00010 and the National Science Foundation (EAR-1763499).

Appendix A

A.1. Singular crack

The near-tip stress field as given by Eq. (1) is related to the fracture energy through Eq. (2). The rupture speed and material wave-speeds provide the following relations

$$\alpha_s = \sqrt{1 - C_f^2/C_s^2} \tag{A.1}$$

$$\alpha_d = \sqrt{1 - C_f^2/C_d^2}\,. \tag{A.2}$$

The Rayleigh function is given by

$$D(C_f) = 4\alpha_s\alpha_d - (1+\alpha_s^2)^2\,, \tag{A.3}$$

and the universal function of crack tip speed as it appears in Eq. (2) is given by

$$f_{\mathrm{II}}(C_f) = \frac{\alpha_s}{(1-\nu)D}\frac{C_f^2}{C_s^2}\,. \tag{A.4}$$

The angular variation is given by

$$\Sigma_{xy}^{\mathrm{II}}(\theta, C_f) = \frac{1}{D}\left[4\alpha_d\alpha_s\frac{\cos\theta_d/2}{\sqrt{\gamma_d}} - (1+\alpha_s^2)^2\frac{\cos\theta_s/2}{\sqrt{\gamma_s}}\right] \tag{A.5}$$

with

$$\theta_s = \arctan\left(\alpha_s\tan\theta\right) \tag{A.6}$$

$$\theta_d = \arctan\left(\alpha_d\tan\theta\right) \tag{A.7}$$

$$\gamma_s = \sqrt{1 - \left(\frac{C_f}{C_s}\sin\theta\right)} \tag{A.8}$$

$$\gamma_d = \sqrt{1 - \left(\frac{C_f}{C_d}\sin\theta\right)} \tag{A.9}$$

Note that the angular variation, Eq. (A.5), is independent of the fracture energy.

A.2. Cohesive crack

This section summarizes the relation between the stress fields around a cohesive crack and local properties Γ and X_c of a cohesive zone. We focus, for simplicity, on a linear cohesive zone by following Poliakov et al. (2002). A more general solution can be found in Samudrala et al. (2002).

We define the following complex variables:

$$z_s = x + i\alpha_s y \tag{A.10}$$

$$z_d = x + i\alpha_d y\,. \tag{A.11}$$

The local peak strength is computed by

$$\tau_p - \tau_r = \sqrt{\frac{\Gamma E}{(1-\nu^2)f_{\mathrm{II}}}}\sqrt{\frac{9\pi}{32X_c}}\,, \tag{A.12}$$

where the first term corresponds to the stress intensity factor that is substituted by Eq. (2), and f_{II} is given by Eq. (A.4). For a linear cohesive zone, as given by Eq. (3), we define an analytic function

$$M(z) = \frac{\tau_p - \tau_r}{\pi}\left[\left(1+\frac{z}{X_c}\right)\arctan\left(\frac{z}{X_c}\right)^{-1/2} - \left(\frac{z}{X_c}\right)^{1/2}\right]\,, \tag{A.13}$$

and compute the shear stress field as

$$\Delta\sigma_{xy}(x,y) = \Re\left[4\alpha_s\alpha_d M(z_d) - (1+\alpha_s^2)^2 M(z_s)\right]/D\,, \tag{A.14}$$

where $\Re$ is the real part of a complex number. Examples of the shear stress along the fault ($y=0$) are shown in Fig. 2 and Fig. 3.

References

Abercrombie, R.E., Rice, J.R., 2005. Can observations of earthquake scaling constrain slip weakening? Geophys. J. Int. 162, 406–424. https://doi.org/10.1111/j.1365-246X.2005.02579.x.

Bayart, E., Svetlizky, I., Fineberg, J., 2016. Fracture mechanics determine the lengths of interface ruptures that mediate frictional motion. Nat. Phys. 12, 166–170. https://doi.org/10.1038/NPHYS3539.

Beeler, N., Kilgore, B., McGarr, A., Fletcher, J., Evans, J., Baker, S.R., 2012. Observed source parameters for dynamic rupture with non-uniform initial stress and relatively high fracture energy. J. Struct. Geol. 38, 77–89. https://doi.org/10.1016/j.jsg.2011.11.013.

Bhat, H.S., Dmowska, R., King, G.C.P., Klinger, Y., Rice, J.R., 2007. Off-fault damage patterns due to supershear ruptures with application to the 2001 Mw 8.1 Kokoxili (Kunlun) Tibet earthquake. J. Geophys. Res., Solid Earth 112. https://doi.org/10.1029/2006JB004425.

Bizzarri, A., Cocco, M., 2003. Slip-weakening behavior during the propagation of dynamic ruptures obeying rate- and state-dependent friction laws. J. Geophys. Res. 108, 2373. https://doi.org/10.1029/2002JB002198.

Broberg, K., 1994. Intersonic bilateral slip. Geophys. J. Int. 119, 706–714. https://doi.org/10.1111/j.1365-246X.1994.tb04010.x.

Broberg, K.B., 1989. The near-tip field at high crack velocities. Int. J. Fract. 39, 1–13. https://doi.org/10.1007/BF00047435.

Chang, J.C., Lockner, D.A., Reches, Z., 2012. Rapid acceleration leads to rapid weakening in earthquake-like laboratory experiments. Science 338, 101–105.

Di Toro, G., Han, R., Hirose, T., De Paola, N., Nielsen, S., Mizoguchi, K., Ferri, F., Cocco, M., Shimamoto, T., 2011. Fault lubrication during earthquakes. Nature 471, 494–498. https://doi.org/10.1038/nature09838.

Dieterich, J.H., 1979. Modeling of rock friction, 1: experimental results and constitutive equations. J. Geophys. Res. 84, 2161–2168.

Dieterich, J.H., 1981. Potential for geophysical experiments in large scale tests. Geophys. Res. Lett. 8, 653–656.

Dunham, E., Archuleta, R., 2005. Near-source ground motion from steady state dynamic rupture pulses. Geophys. Res. Lett. 32. https://doi.org/10.1029/2004GL021793.

Dunham, E.M., Belanger, D., Cong, L., Kozdon, J.E., 2011. Earthquake ruptures with strongly rate-weakening friction and off-fault plasticity, part 2: nonplanar faults. Bull. Seismol. Soc. Am. 101, 2308–2322. https://doi.org/10.1785/0120100076.

Freund, L., 1990. Dynamic Fracture Mechanics. Cambridge University Press, New York.

Fukuyama, E., Xu, S., Yamashita, F., Mizoguchi, K., 2016. Cohesive zone length of metagabbro at supershear rupture velocity. J. Seismol. 20 (4), 1207–1215. https://doi.org/10.1007/s10950-016-9588-2.

Galvez, P., Dalguer, L.A., Ampuero, J.P., Giardini, D., 2016. Rupture reactivation during the 2011 Mw 9.0 Tohoku earthquake: dynamic rupture and ground-motion simulations. Bull. Seismol. Soc. Am. 106, 819–831. https://doi.org/10.1785/0120150153.

Guatteri, M., Spudich, P., 2000. What can strong-motion data tell us about slip-weakening fault-friction laws? Bull. Seismol. Soc. Am. 90, 98. https://doi.org/10.1785/0119990053.

Ishii, M., 2011. High-frequency rupture properties of the Mw 9.0 off the Pacific coast of Tohoku earthquake. Earth Planets Space 63, 609–614. https://doi.org/10.5047/eps.2011.07.009.

Kammer, D.S., Radiguet, M., Ampuero, J.P., Molinari, J.F., 2015. Linear elastic fracture mechanics predicts the propagation distance of frictional slip. Tribol. Lett. 57. https://doi.org/10.1007/s11249-014-0451-8.

Kammer, D.S., Svetlizky, I., Cohen, G., Fineberg, J., 2018. The equation of motion for supershear frictional rupture fronts. Sci. Adv. 4, 12784–12792. https://doi.org/10.1126/sciadv.aat5622.

Ke, C.Y., McLaskey, G.C., Kammer, D.S., 2018. Rupture termination in laboratory-generated earthquakes. Geophys. Res. Lett. 45, 12–784. https://doi.org/10.1029/2018GL080492.

Latour, S., Voisin, C., Renard, F., Larose, E., Catheline, S., Campillo, M., 2013. Effect of fault heterogeneity on rupture dynamics: an experimental approach using ultrafast ultrasonic imaging. J. Geophys. Res., Solid Earth 118, 5888–5902. https://doi.org/10.1002/2013JB010231.

Lu, X., Lapusta, N., Rosakis, A.J., 2007. Pulse-like and crack-like ruptures in experiments mimicking crustal earthquakes. Proc. Natl. Acad. Sci. USA 104, 18931–18936. https://doi.org/10.1073/pnas.0704268104.

Lykotrafitis, G., Rosakis, A.J., Ravichandran, G., 2006. Self-healing pulse-like shear ruptures in the laboratory. Science 313, 1765–1768. https://doi.org/10.1126/science.1128359.

McLaskey, G.C., Kilgore, B.D., 2013. Foreshocks during the nucleation of stick-slip instability. J. Geophys. Res., Solid Earth 118, 2982–2997. https://doi.org/10.1002/jgrb.50232.

McLaskey, G.C., Kilgore, B.D., Beeler, N.M., 2015. Slip-pulse rupture behavior on a 2 m granite fault. Geophys. Res. Lett. 42, 7039–7045. https://doi.org/10.1002/2015GL065207.

Mello, M., Bhat, H.S., Rosakis, A.J., Kanamori, H., 2010. Identifying the unique ground motion signatures of supershear earthquakes: theory and experiments. Tectonophysics 493, 297–326. https://doi.org/10.1016/j.tecto.2010.07.003.

Meng, L., Huang, H., Bürgmann, R., Ampuero, J.P., Strader, A., 2015. Dual megathrust slip behaviors of the 2014 Iquique earthquake sequence. Earth Planet. Sci. Lett. 411, 177–187.

Meng, L., Inbal, A., Ampuero, J.P., 2011. A window into the complexity of the dynamic rupture of the 2011 Mw 9 Tohoku-Oki earthquake. Geophys. Res. Lett. 38, L00G07. https://doi.org/10.1029/2011GL048118.

Mitiyasu, O., Lin-feng, S., 1999. Scaling of the shear rupture process from nucleation to dynamic propagation: implications of geometric irregularity of the rupturing surfaces. J. Geophys. Res., Solid Earth 104, 817–844. https://doi.org/10.1029/1998JB900007.

Nielsen, S., Spagnuolo, E., Smith, S.A.F., Violay, M., Di Toro, G., Bistacchi, A., 2016a. Scaling in natural and laboratory earthquakes. Geophys. Res. Lett. 43, 1504–1510. https://doi.org/10.1002/2015GL067490.

Nielsen, S., Spagnuolo, E., Violay, M., Smith, S., Di Toro, G., Bistacchi, A., 2016b. G: fracture energy, friction and dissipation in earthquakes. J. Seismol. 20, 1187–1205. https://doi.org/10.1007/s10950-016-9560-1.

Ohnaka, M., Kuwahara, Y., 1990. Characteristic features of local breakdown near a crack-tip in the transition zone from nucleation to unstable rupture during stick-slip shear failure. Tectonophysics 175, 197–220. https://doi.org/10.1016/0040-1951(90)90138-X.

Okubo, P.G., Dieterich, J.H., 1984. Effects of physical fault properties on frictional instabilities produced on simulated faults. J. Geophys. Res., Solid Earth 89, 5817–5827. https://doi.org/10.1029/JB089iB07p05817.

Poliakov, A.N.B., Dmowska, R., Rice, J.R., 2002. Dynamic shear rupture interactions with fault bends and off-axis secondary faulting. J. Geophys. Res., Solid Earth 107, 2295. https://doi.org/10.1029/2001JB000572.

Rice, J.R., 2005. Off-fault secondary failure induced by a dynamic slip pulse. Bull. Seismol. Soc. Am. 95, 109. https://doi.org/10.1785/0120030166.

Rubino, V., Rosakis, A.J., Lapusta, N., 2017. Understanding dynamic friction through spontaneously evolving laboratory earthquakes. Nat. Commun. 8, 15991. https://doi.org/10.1038/ncomms15991.

Rubinstein, S., Cohen, G., Fineberg, J., 2007. Dynamics of precursors to frictional sliding. Phys. Rev. Lett. 98, 226103. https://doi.org/10.1103/PhysRevLett.98.226103.

Ruina, A.L., 1983. Slip instability and state variable friction laws. J. Geophys. Res. 88, 10359. https://doi.org/10.1029/JB088iB12p10359.

Samudrala, O., Huang, Y., Rosakis, A.J., 2002. Subsonic and intersonic shear rupture of weak planes with a velocity weakening cohesive zone. J. Geophys. Res., Solid Earth 107, 7. https://doi.org/10.1029/2001JB000460.

Shi, Z., Day, S.M., 2013. Rupture dynamics and ground motion from 3-d rough-fault simulations. J. Geophys. Res., Solid Earth 118, 1122–1141. https://doi.org/10.1002/jgrb.50094.

Svetlizky, I., Fineberg, J., 2014. Classical shear cracks drive the onset of dry frictional motion. Nature 509, 205–208. https://doi.org/10.1038/nature13202.

Svetlizky, I., Kammer, D.S., Bayart, E., Cohen, G., Fineberg, J., 2017. Brittle fracture theory predicts the equation of motion of frictional rupture fronts. Phys. Rev. Lett. 118, 125501. https://doi.org/10.1103/PhysRevLett.118.125501.

Svetlizky, I., Pino Muñoz, D., Radiguet, M., Kammer, D.S., Molinari, J.F., Fineberg, J., 2016. Properties of the shear stress peak radiated ahead of rapidly accelerating rupture fronts that mediate frictional slip. Proc. Natl. Acad. Sci. USA 113, 542–547. https://doi.org/10.1073/pnas.1517545113.

Tinti, E., Spudich, P., Cocco, M., 2005. Earthquake fracture energy inferred from kinematic rupture models on extended faults. J. Geophys. Res., Solid Earth 110, B12303. https://doi.org/10.1029/2005JB003644.

Viesca, R.C., Garagash, D.I., 2015. Ubiquitous weakening of faults due to thermal pressurization. Nat. Geosci. 8, 875–879. https://doi.org/10.1038/NGEO2554.

Xia, K., Rosakis, A.J., Kanamori, H., 2004. Laboratory earthquakes: the sub-Rayleigh-to-supershear rupture transition. Science 303, 1859–1861. https://doi.org/10.1126/science.1094022.

Xu, S., Fukuyama, E., Yamashita, F., Mizoguchi, K., Takizawa, S., Kawakata, H., 2017. Strain rate effect on fault slip and rupture evolution: insight from meter-scale rock friction experiments. Tectonophysics.